An ice-ocean model study of the mid-2000s regime change in the Barents Sea

Benjamin I. Barton, Camille Lique, Yueng-djern Lenn, Claude Talandier

JGR Oceans

RESEARCH ARTICLE
10.1029/2021JC018280

An Ice-Ocean Model Study of the Mid-2000s Regime Change in the Barents Sea

Benjamin I. Barton[1,2,3], Camille Lique[2], Yueng-Djern Lenn[3], and Claude Talandier[2]

[1]National Oceanography Centre, Liverpool, UK, [2]Laboratoire d'Océanographie Physique et Spatiale (LOPS), CNRS, IRD, Ifremer, University of Brest, IUEM, Brest, France, [3]Bangor University, Bangor, UK

Key Points:

- We identify events of minimum dense water volume in the Barents Sea, with the 2002–2005 event being unique with large sea ice import
- During this event, a freshwater anomaly from sea ice melt enhanced the salinity gradient, reducing dense water formation and export
- After the event in 2006–2014, the proportion of dense water present in the southern Barents Sea remained smaller than during 1985–2002

Correspondence to:

B. I. Barton,
benbar@noc.ac.uk

Citation:

Barton, B. I., Lique, C., Lenn, Y.-D., & Talandier, C. (2022). An ice-ocean model study of the mid-2000s regime change in the Barents Sea. *Journal of Geophysical Research: Oceans*, *127*, e2021JC018280. https://doi.org/10.1029/2021JC018280

Received 24 NOV 2021
Accepted 18 OCT 2022

Author Contributions:

Conceptualization: Benjamin I. Barton, Camille Lique, Yueng-Djern Lenn
Data curation: Claude Talandier
Formal analysis: Benjamin I. Barton
Funding acquisition: Camille Lique, Yueng-Djern Lenn
Investigation: Benjamin I. Barton
Methodology: Benjamin I. Barton, Camille Lique, Yueng-Djern Lenn
Project Administration: Camille Lique, Yueng-Djern Lenn
Resources: Claude Talandier
Software: Benjamin I. Barton, Claude Talandier
Supervision: Camille Lique, Yueng-Djern Lenn
Validation: Benjamin I. Barton
Visualization: Benjamin I. Barton
Writing – original draft: Benjamin I. Barton

Abstract Over the satellite record, the Barents Sea winter maximum in sea ice extent has declined and was increasingly limited to areas north of the Polar Front after 2005 by warming Atlantic Water (AW) and Barents Sea Water (BSW). Sea ice extent here continues to garner interest, not least because it is associated with extreme winter weather in Europe and Asia. Previous model studies suggest there is a possibility that natural variability will cause southward re-expansion of the lost sea ice cover but reducing uncertainties requires a better understanding of the processes driving BSW variability. To address questions about BSW variability, we used a high-resolution model validated with observations over 1985–2014 to calculate the watermass transport, heat, and freshwater budgets within the central Barents Sea, south of the Polar Front. The model shows BSW volume minima events in years centering at 1990 and 2004, meaning a reduction in the Barents Sea's volume reservoir (also termed "memory") of water that is consistent with historical BSW properties. Both events were preceded by extensive winter sea ice and substantial summer net sea ice melt. The event in 2004 was more extreme and led to warming AW occupying a greater volume in the Barents Sea after 2005. The reduced "memory" of BSW volume could impede a return to the more extensive winter sea ice regime and make further reduction in winter sea ice possible.

Plain Language Summary Winter sea ice in the Barents Sea, in the eastern Arctic Ocean, has been in decline, particularly since 2000. The sea ice extent in this region is associated with atmospheric weather conditions during winter in Europe and Asia. An important factor in understanding the sea ice retreat is understanding the variability in Barents Sea temperature and salinity. Using a high-resolution simulation, the source of variability in Barents Sea Water (BSW) properties has been quantified. This shows two events, 1990 and 2004, when BSW volume reduced, giving less "memory" of previous conditions. The event in 2004 was larger and followed a large net sea ice melt. The volume of BSW present in the Barents Sea did not fully recover after 2005. This could make it more difficult for winter sea ice to return to the region.

1. Introduction

The Barents Sea experienced a 50% reduction in annual sea ice extent between 1998 and 2008 (Årthun et al., 2012). Over the satellite record from 1979 to present, both the summer minimum and winter maximum in sea ice extent have receded, leaving the Barents Sea mostly ice free in summer (Onarheim & Årthun, 2017; Onarheim et al., 2018). Following a notable increase in inflowing Atlantic Water (AW) temperatures in the mid-2000s and beyond, the Barents Sea winter sea ice no longer extends south of the polar front due to the presence of significantly warmer water south of the front (Barton et al., 2018). The changes in sea ice here are important because they have been associated with extreme weather patterns in Europe and Asia (Luo et al., 2016; Petoukhov & Semenov, 2010), and may foreshadow future conditions in the central Arctic. Although the physics of the relationship between sea ice and weather patterns is still an area of active research (e.g., Blackport & Screen, 2021; Blackport et al., 2019; McCrystall & Screen, 2021; Warner et al., 2020), it is commonly accepted that, on short time scales (days to months) the atmosphere forces the sea ice extent (Gong & Luo, 2017), while longer-term variability in sea ice extent may be driven by the ocean (Hoshi et al., 2019).

In addition to AW, the Barents Sea has two other main watermasses. These are Barents Sea Water (BSW) and Arctic Water (ArW). The mean locations where AW, BSW, and ArW are found are shown on Figure 1, with the surface outcropping of the distinct watermasses separated by fronts. The property definitions of these watermasses can be found in Table 1 and Figure 2 (Barton et al., 2018; Loeng, 1991; Oziel et al., 2016). AW is advected into the Barents Sea through the southern end of the Barents Sea Opening between Fugløya, Norway and Bear

Writing – review & editing: Benjamin I. Barton, Camille Lique, Yueng-Djern Lenn, Claude Talandier

Island (Ingvaldsen et al., 2004b). Some of this AW recirculates within the western Barents Sea and exits through the northern end of the Barents Sea Opening. Most of the remaining AW is advected eastward into the Central Basin where modified AW is found, now known as BSW. Some surface water is transformed into ArW with the addition of freshwater. Watermass properties imply that the AW-to-BSW transformation involves slight freshening from various freshwater sources and cooling through atmospheric heat loss during winter (Figure 2) (Oziel et al., 2016). ArW also enters the Barents Sea from the north and northeast between Svalbard, Franz-Josef Land and Novaya Zemlya, forming a salinity-stratified surface layer of relatively freshwater that is present throughout the year in the Northern Barents Sea (Lind et al., 2016). In return, BSW flows northward below the ArW, exiting the Barents Sea through the Barents Sea Exit between Franz-Josef Land and Novaya Zemlya (Gammelsrød et al., 2009). Understanding the variability and long term changes in BSW properties is particularly important because BSW is advected into the Arctic Basin and can potentially make up 50%–80% of Arctic Intermediate Water volume (Maslowski et al., 2004; Rudels et al., 2000), before contributing to the deeper branch of Atlantic Meridional Overturning Circulation once it is advected back to the North Atlantic through Fram Strait (Fahrbach et al., 2001; Karcher et al., 2011; Le Bras et al., 2021).

Interannual variability in BSW density stems from variability in both heat and freshwater content (Barton et al., 2020). In addition to variability on interannual time-scales, observations have revealed that temperature in the Barents Sea varies on multidecadal time-scales with periodicities of about 6, 10, 18, and 40 years (Levitus et al., 2009; Skagseth et al., 2008; Venegas & Mysak, 2000), while salinity may have periods of variability of about 5 and 10 years (Skagseth, 2008; Yashayaev & Seidov, 2015). These shorter variations come from coupled ocean-atmosphere modes such as anomalies in ocean gyres or the North Atlantic Oscillation. Longer term variations may come from the Atlantic Multidecadal Oscillation (Levitus et al., 2009), although this may be the result of anthropogenic and natural forcing rather than an internal oscillation (Mann et al., 2020). Based on the analysis of available in situ and satellite observations, Barton et al. (2018) showed that BSW temperature and salinity had increased between 1985–2004 and 2005–2016 when the sea ice declined, a shift with an amplitude that may have exceeded amplitudes of multidecadal variability cycles. These changes have been observed to cause northward expansion of oceanic boreal species (Fossheim et al., 2015; Ingvaldsen et al., 2021). If the natural variability of the Barents Sea is to reassert its influence, climate projections from an ensemble of models show there is a 40% possibility of winter sea ice cover increasing its extent in the south-eastern Barents Sea by 2040 instead of a continuation of the decline seen between 2000 and 2015 (Årthun et al., 2019).

Clearly, strong variability in BSW properties exists but the mechanisms driving this variability remain elusive (Barton et al., 2018, 2020). It has been suggested that the 2005 apparent regime change was caused by a warming of AW but we lack the observations to resolve the ocean processes leading to the 2005 regime change or the processes at play for the formation of BSW from AW more generally (Loeng, 1991; Schauer et al., 2002). Numerical models allow us to identify and quantify the processes resulting in BSW watermass transformation (Aksenov et al., 2010; Årthun et al., 2011). This will improve our understanding of the drivers that determine if the winter sea ice will expand, return to the previous regime or if a tipping point has been irreversibly passed and a further step change reduction in sea ice could occur.

In this study, we investigate the drivers of the seasonal to interannual variability in AW and BSW volume and properties in the central Barents Sea. More specifically, we try to determine how the regime change happened in 2005, and how a further reduction in sea ice and BSW could happen again in the future. We will answer these questions by analyzing model outputs from a high-resolution model of the pan-Arctic region, focusing on the Barents Sea region. In Section 2, we describe the model set-up and validate the simulation with available satellite and in situ observations. In Section 3, we calculate the advective heat and freshwater budgets for the Barents Sea, and relate these budgets to the variability of the properties of the different watermasses present within the Barents Sea. In Section 4, we place the 2002–2005 event in a broader temporal context and more particularly compare it with a similar event that occurred in 1987–1991. We discuss the results in Section 5, and our conclusions are given in Section 6.

2. Data and Methods

2.1. Model Simulation

In this paper, we used model output to analyze the heat and freshwater budgets and variability of watermass properties in the Barents Sea. The model is a regional configuration of the Arctic and North Atlantic Oceans, named

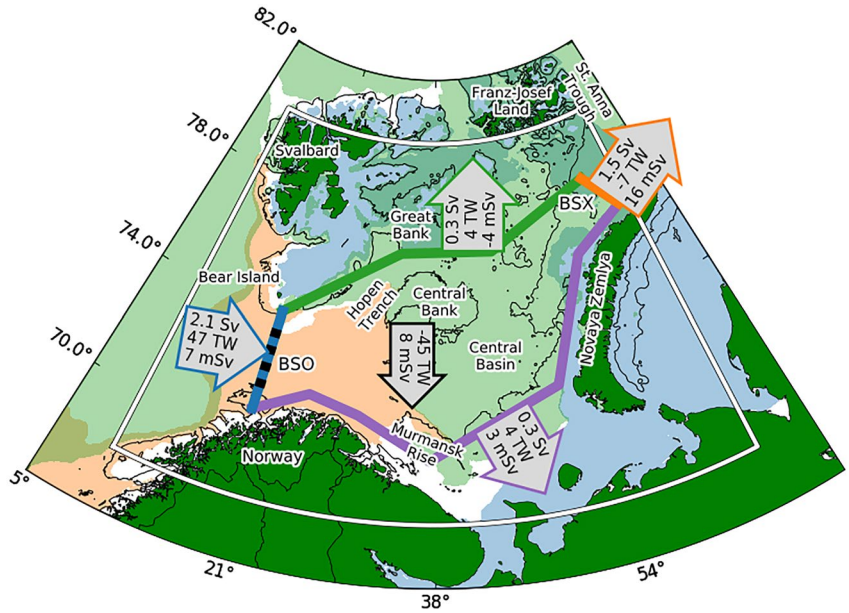

Figure 1. Box for budget calculation shown as region bounded by blue, green, purple, and orange lines. Lines show boundaries (blue = West, green = North, orange = East, and purple = South). Orange, green and blue shading show the regions with Atlantic Water, Barents Sea Water (BSW), and Arctic Water volume filling >30% of the water column, respectively. Note, the green shaded region in the Norwegian Sea (west of 20°E) is deep BSW that has submerged to form Arctic Intermediate Water and is exiting the Arctic Ocean through Fram Strait. The thick black dashed line shows position of the mooring array across the Barents Sea Opening (the Fugløya–Bear Island section along 20.0°E). White line indicates the region use to estimate the sea ice extent for Figure 3. BSO is the Barents Sea Opening and BSX is the Barents Sea Exit. The annotated colored arrows show mean transport (in Sv), mean heat flux (in TW) and mean freshwater flux (in mSv) across each respective boundary from the model. The annotated black arrow shows downward mean surface heat flux (in TW) and mean sea ice freshwater flux (in mSv) into the budget box. The solid black contour lines indicates the 220 m isobath.

CREG12 (Canadian Regional; Dupont et al., 2015; Regan et al., 2020). This is based on the ocean model NEMO (Nucleus for European Modeling of the Ocean (Madec & The_NEMO_Team, 2008)). The sea ice coupling component of CREG12 is LIM3 (Rousset et al., 2015). Model resolution is 1/12° which is ~4.3 km by 5–4 km in the Barents Sea on the irregular grid named ORCA12. This grid resolution is not high enough to resolve mesoscale features here, which have spatial scales of a few kilometers (Nurser & Bacon, 2014). The model has 75 depth levels, of which 36 depth levels resolve the 330 m of the Barents Sea continental shelf.

Table 1
Table of Watermass Properties Used for the Observations and the Simulation

Watermass	Temperature	Salinity	Density
AW Observations	$T > 3$°C	$S > 34.8$ PSU	
AW Model	$T > 3$°C	$S > 34.7$ PSU	
BSW Observations	$T < 2$°C	$S > 34.7$ PSU	$\rho > 1{,}027.85$
BSW Model	$T < 2$°C	$S > 34.6$ PSU	$\rho > 1{,}027.77$
ArW Observations	$T < 0$°C	$S < 34.7$ PSU	
ArW Model	$T < 0$°C	$S < 34.6$ PSU	

Note. Observations use standard definition but the model uses updated definitions to account for the 0.1 PSU fresh salinity bias in the model. Temperature is potential temperature, salinity is in practical salinity units (PSU) and density is surface referenced potential density.

We took initial conditions from the World Ocean Atlas 2009 climatology for temperature and salinity while the ocean is at rest (Antonov et al., 2010; Locarnini et al., 2010). The initial sea ice thickness and concentration were taken from a long ORCA12 simulation performed by the Drakkar Group (Barnier et al., 2006; Treguier et al., 2014). At lateral open boundaries along 26°N in the Atlantic and across the Bering Strait, monthly climatological conditions (comprising 3-D velocities, temperature and salinity) were taken from the same ORCA12 simulation. For atmospheric forcing, we used the latest version of the Drakkar Forcing Set (DFS5.2, which is an updated version of the forcing set described in Brodeau et al., 2010). Inputs from the river and ice sheet runoff have been recently corrected to include the large and increasing contribution from Greenland (Gillard et al., 2016). The representation of the tidal mixing effect was activated through the new comprehensive parameterization of mixing by breaking internal tides and lee waves (de Lavergne et al., 2019). We have a weak sea surface salinity restoring toward the monthly climatological sea surface salinity from World Ocean Atlas 2009 in ice free areas to avoid a model salinity drift while, under sea ice, this sea surface salinity restoring is turned off. The simulation covers the

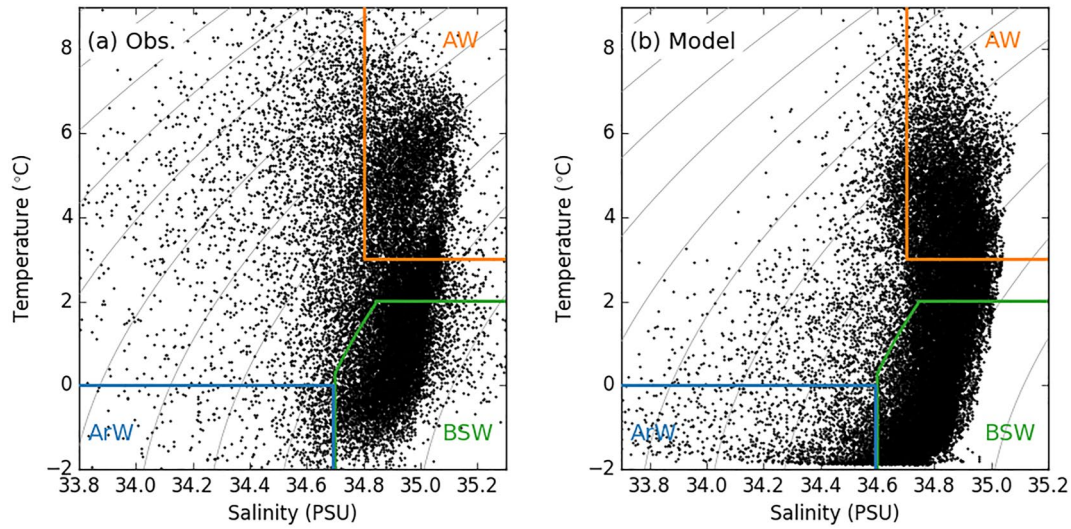

Figure 2. T/S diagram showing the relevant watermass properties. The orange box is Atlantic Water, the green box is Barents Sea Water and the blue box is Arctic Water. (a) Shows in situ observations from EN4. (b) Shows model output from the simulation used in this study. The black points are a collection of locations and depths in the central Barents Sea budget box (see area contained between blue, green, purple and orange lines on Figure 1) over the time period 1985–2015. Both model and EN4 data is binned onto a grid with resolution 5° in longitude, 3° in latitude and depth levels at 5, 55, 110, 185, and 373 m.

period 1979–2015, although we only analyzed years 1985–2015 to allow for model spin up in the first 6 years. The analysis we present here is based on monthly-mean model output. The description of the simulation is given by Talandier and Lique (2021). The same simulation was used by Regan et al. (2020) and Meneghello et al. (2021) to investigate some aspects of the Arctic dynamics and was found to realistically represent the properties of the large and small scale circulations within the Arctic Basin.

2.2. Observational Data Sets

The realism of the simulation is assessed by comparing the model outputs with the following observation data sets. We used satellite sea surface temperature (SST) and sea ice concentration data sets from the OSTIA project spanning January 1985 to December 2016 (downloaded from marine.copernicus.eu portal; Donlon et al., 2012). This data set is optimally interpolated from multiple satellite sensors together with in situ observations onto a 0.05° grid (1.5 × 5.6 km for Barents Sea) at a daily frequency. The feature resolution is 10 km and the accuracy of the daily SST data is ~0.57 K (Donlon et al., 2012). The sea ice edge is defined as the 15% contour.

We also used observations of AW inflow transport and associated heat transport from the Fugløya–Bear Island section along 20.0°E (which corresponds to the Barents Sea Opening; black dashed line Figure 1). This data set is available through the Norwegian Marine Data Centre portal (www.nmdc.no) and is compiled as monthly means from long-term current meter moorings for the period 1997–2016. The time series is built by averaging the part of the section below 50 m between 71.5°N and 73.5°N where there is an inflow, and only considering the part of the water columnwith $T > 3$°C (Ingvaldsen et al., 2004a, 2021). We computed a comparable section using the same criteria based on our simulation.

We analyzed temperature and salinity fields from the data set named EN4 (EN4.2.0, www.metoffice.gov.uk/hadobs/en4). EN4 comprises in situ ship CTD profile data and Argo float data optimally interpolated onto a 1°, monthly z-grid with 42 levels (Gouretski & Reseghetti, 2010). Data are available from January 1980 to December 2016. Within the Barents Sea (10°E–65°E and 68°N–80°N) over this time frame, each 3-month period has more than 117 profiles. The sampling density of profiles is, however, biased toward September, October and November (when there are usually more than 400 profiles) and toward the ice-free part of the Barents Sea.

2.3. Methods

To calculate budgets of heat and freshwater, we defined a box within the Barents Sea (Figure 1). The change in the heat budget (total heat flux) Q_t can be calculated from ocean advective heat transport Q_{adv} and surface heat flux Q_{surf} in Equation 1 (Serreze et al., 2007).

$$Q_t = Q_{adv} + Q_{surf} \tag{1}$$

Similarly, we estimated a change in the freshwater budget (total freshwater flux) F_t for the same box where F_{adv} is the freshwater advective transport. In this case, the freshwater surface flux F_{surf} corresponds to the contribution of evaporation minus precipitation, river runoff and from sea ice processes. Equation 2 is the freshwater budget (Serreze et al., 2006).

$$F_t = F_{adv} + F_{surf} \tag{2}$$

We calculated heat advection from transport across the different sections closing the box as $Q_{adv} = \iint \rho C_p (T - T_{ref}) V\, dx\, dz$, where C_p is the specific heat capacity of seawater, ρ is the water density, V is the velocity normal to the section, T is the temperature and T_{ref} is a reference temperature taken as 0°C following Årthun and Schrum (2010). For the transport calculations, we used the CDFTOOLS package designed to work on NEMO model grids including ORCA12 (see https://github.com/meom-group/CDFTOOLS). The surface heat flux was calculated as $Q_{surf} = Q_{sw} - Q_{lw} - Q_{lat} - Q_{sen}$ net shortwave (i.e., solar) (Q_{sw}) and net longwave (i.e., infrared) (Q_{lw}) radiative fluxes, and surface turbulent latent Q_{lat} and sensible Q_{sen} heat fluxes. These parameters were integrated over the surface area of the same box, which has a total area 6.1×10^{11} m^2 (Figure 1). The integrated fluxes follow the convention where positive values represent flux into the ocean.

We calculated freshwater transport as $F_{adv} = \iint ((S_{ref} - S)/S_{ref}) V\, dx\, dz$, where S is salinity in PSU (practical salinity units) and S_{ref} is a reference salinity taken as 35 PSU (Smedsrud et al., 2010). Here we considered both negative and positive contributions. The surface freshwater flux was calculated as $F_{surf} = E - P + R + i_{melt}$, where E is evaporation, P is precipitation, R is river runoff and i_{melt} is freshwater from sea ice melting and freezing processes. In this manuscript we often refer to net sea ice melt which is the melt minus freeze. The freshwater flux from net sea ice melt i_{melt} includes the salinity of sea ice in the calculation. Again, positive values for the integrated fluxes represent flux into the ocean.

We calculated sea ice transport using a similar method to the ocean boundary transport. For sea ice transport, we used the sum of sea ice thickness H_{ice} and snow thickness H_{snow} multiplied by the sea ice concentration α_{ice} and sea ice velocity V_{ice} across the boundaries as $I = \int (H_{ice} + H_{snow}) \alpha_{ice} V_{ice}\, dx$.

We also derived a closed budget for the different watermasses found within the box. Equation 3 calculates M the change in buoyancy forcing exerted on the watermasses found within our budget box volume that is, watermass transformation, by combining watermass volume change ψ_t, the surface volume flux Ψ_{surf} (in our case evaporation minus precipitation and net sea ice import) and the advective watermass convergence $\Delta\Psi_{adv}$ (Nurser et al., 1999).

$$M = \psi_t - \Psi_{surf} - \Delta\Psi_{adv} \tag{3}$$

Watermass transports were calculated in a similar way to the heat transport using the volume transport on grid cells matching the watermass property criteria in Table 1. We focused on AW, BSW, and ArW in this study; however to close our total budgets we also calculated the budget for other water that does not meet the properties criteria of AW, BSW, and ArW. These transports and volume change can be used to calculate watermass transformation due to the closed budget. Watermass properties in the Barents Sea region are changing because the Arctic is warming. However, in this study we ignored this, instead we focused on fixed definitions and volume changes to those watermasses within this region so that we can be compatible with existing literature. This is because our focus is on the mechanisms driving BSW formation rather than the fact that the whole Arctic and its watermasses are in transition.

Mixed layer depth was calculated while the model ran, from a 0.01 kg m^{-3} change in density relative to the density at 10 m depth. We identified fronts in the simulation as local maxima in the temperature gradients given by $|\nabla T_{(x,y)}| = \sqrt{(\partial T/\partial x)^2 + (\partial T/\partial y)^2}$, and compared with the fronts estimated from satellite observations in

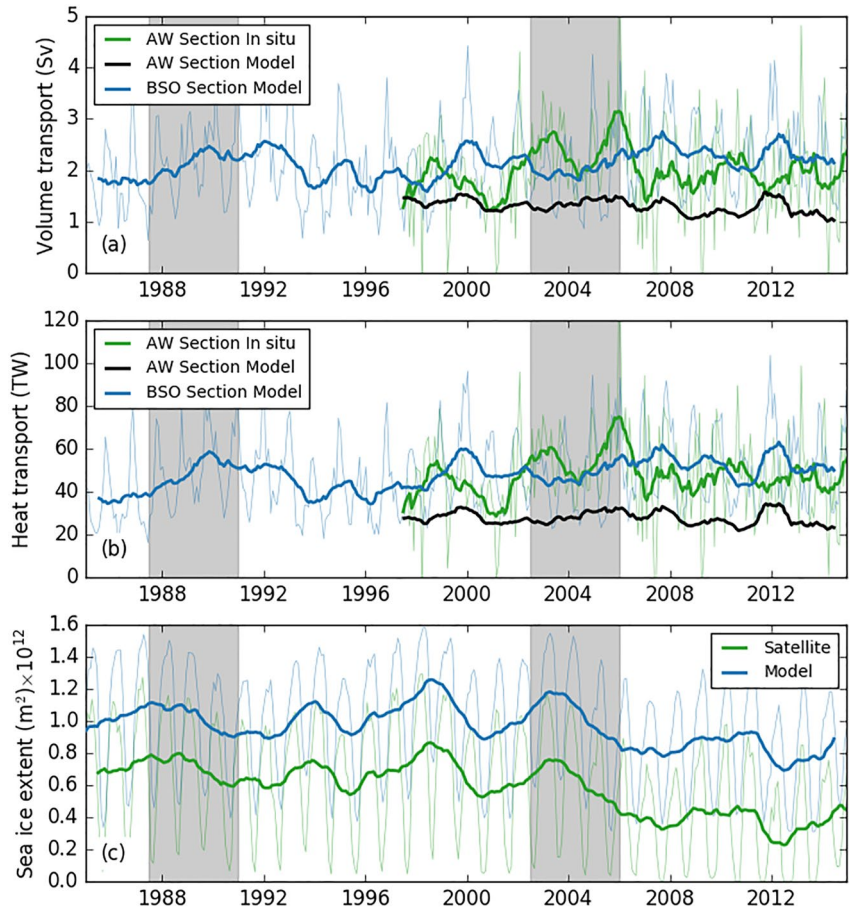

Figure 3. (a) Volume and (b) heat transport through the Barents Sea Opening (Fugløya–Bear Island section along 20.0°E). The green line shows the observations of Atlantic Water transport ($T > 3$°C and depth > 50 m) across the black dashed line in Figure 1, the black line shows the model estimate using the same Atlantic Water definition (See Section 2.3), the blue line shows model estimate across the Barents Sea Opening (Barents Sea Opening, blue line in Figure 1) with depth > 50 m but without a temperature criteria. (c) Sea ice extent within the Barents Sea (68°N–80°N and 10°E–65°E) for model and satellite observations (white line in Figure 1). In all cases, thin line show monthly data and thick lines show 12-month running means. The gray bars highlight periods of interest July 1987 to December 1991 and July 2002 to December 2005 events.

Barton et al. (2018). Here, the results are based on the computation of SST gradients by calculating the seasonal mean of the monthly gradient to resolve sharper fronts instead of the gradient of the seasonal mean.

We calculated the amplitude of interannual variability over the full time period as the standard deviation of the 12-month running mean. The amplitude of the seasonal variability was calculated by subtracting the 12-month running mean from the monthly data and calculating the standard deviation of this. We performed lead-lag least squares regression on monthly running mean data with significance estimated at the 95% level using a two-tailed Student's *t*-test. Effective degrees of freedom were estimated from the decorrelation time-scale (1/e of peak correlation) required to avoid auto-correlation.

2.4. Model Evaluation

We first evaluate the capacity of the model simulation to reproduce the spatio-temporal variability of the ocean and sea ice properties in the Barents Sea as captured by available observations.

The model sea ice extent shows a 0.4×10^{12} m^2 positive bias (mean extent is 0.97×10^{12} m^2) relative to the satellite observations (Figure 3c). This measure of sea ice extent was calculated over the white box in Figure 1. Maps of the sea ice concentration reveal that the model has more sea ice in the coastal southern Barents Sea and over the Central Bank compared to the satellite observations (Figure 4). Despite this bias, the model sea ice

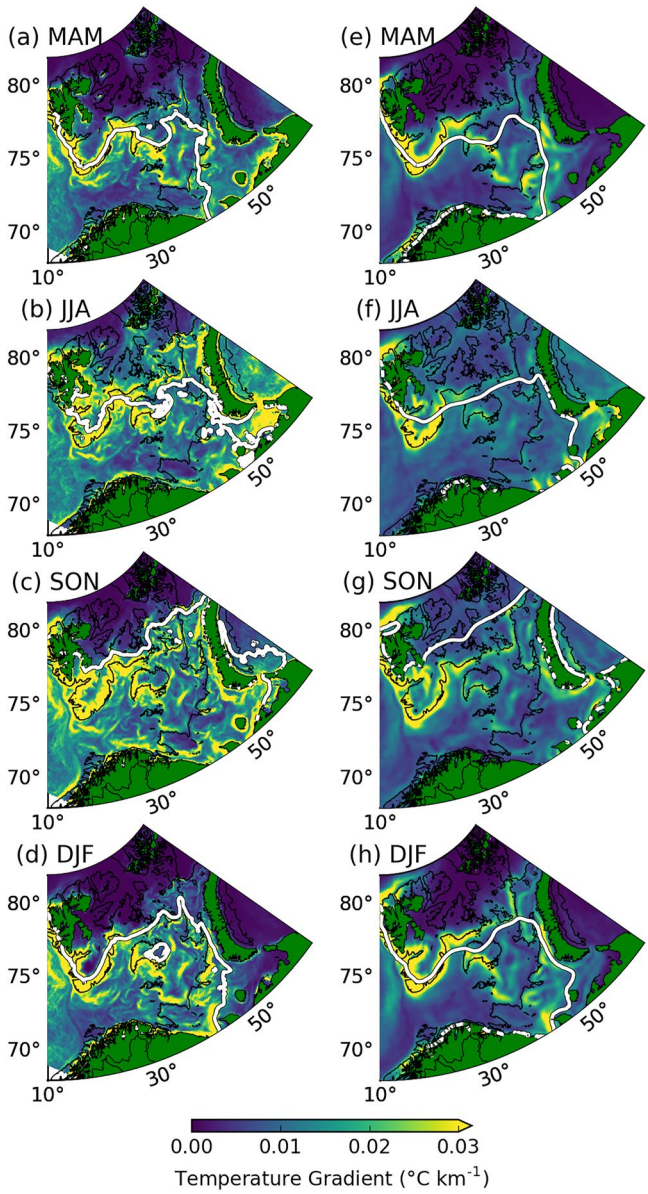

Figure 4. Gradient in sea surface temperature seasonal climatology from 2005 to 2014 for (a, e) spring (March, April, and May), (b, f) summer (June, July, and August), (c, g) autumn (September, October, and November) and (d, h) winter (December, January, and February), respectively, from the simulation (a–d) and satellite observations (e–h). The sea ice edge is defined by 15% sea ice concentration (white line) and the black line indicates the 220 m isobath.

extent exhibits seasonal and interannual variability with similar amplitude and timing to the observations (Figure 3c). The model is also capturing well the observed decline in sea ice in the mid-2000s.

We now examine the capacity of the simulation at representing the observed surface fronts in the Barents Sea, which are known to affect sea ice variability and represent the boundaries the watermasses present in the region (Barton et al., 2018; Oziel et al., 2016). The climatology of the SST gradient calculated over the 2005–2014 time period shows that the locations of the thermal fronts are similar in the model and observations in all seasons (Figure 4). This is particularly important for the polar front that separates the surface outcropping of AW (or BSW) from ArW. Since BSW is not in direct contact with the atmosphere when it is overlain by ArW to the north of the Polar Front, the surface area available for atmospheric and sea ice interactions is constrained by the position of the fronts in observations and the simulation. The realistic location of the front in the model also suggests the model captures well the interaction between the ocean dynamics and the bathymetry. The main fronts in the Barents Sea have been shown to be associated with bathymetric gradients (Barton et al., 2018; Gawarkiewicz & Plueddemann, 1995). In the observations, the winter sea ice retreated north of the Polar Front at 76.5°N after 2005 (Barton et al., 2018). The observed change in sea ice regime after 2005 is also captured by the simulation, albeit somewhat less pronounced. We next evaluate subsurface properties.

The temperature and salinity properties of the watermasses can be summarized in a T-S diagram (Figure 2). Our comparison between the model properties and the observation properties shows the model salinity has a 0.1 PSU fresh bias relative to EN4 when averaged within the box in Figure 1. To account for this bias, we adjusted the watermass definitions for the model by 0.1 PSU to capture the relative variability within the range of the definition properties. The definition used for observations and updated definition for the model properties are shown in Table 1. Given that this bias is also present in AW properties (Figure 2), it suggests the bias is advected into the Barents Sea rather than present due to the excess sea ice shown in Figure 3c. The biases in T-S properties and the sea ice extent could also result, at least partly, from bias in the atmospheric forcing. Despite this bias, the distribution of water properties throughout the time period considered has a similar clustering in T-S space in the simulation and observations (Figure 2). This suggests that the simulation captures well the different watermasses and the variations in the Barents Sea.

We compare estimates of volume and heat transport from moorings across the Barents Sea Opening to the simulation in Figures 3a and 3b. These transport estimates use the AW definition given in Table 1. Figure 3a shows systematically more transport for the observations (green line; average 2.0 Sv) than the simulation (black line; average 1.30 Sv). When using a different definition for AW ($T > 3$°C), Ingvaldsen et al. (2004a) estimated a mean transport of 1.5 Sv from observations, while Skagseth (2008) estimated a transport of 2.0 Sv when considering the whole water column instead of just the part of the section where AW is present. Overall, observations suggest net volume transport through the Barents Sea Opening is 2.3 Sv, with 2.0 Sv of AW inflow, 1.2 Sv of Norwegian Coastal Current transport and roughly 0.9 Sv export of AW recirculation (Skagseth, 2008; Skagseth et al., 2011; Smedsrud et al., 2013). Any potential systematic biases due to applying the constraints of the width of the observation section on the model were eliminated by choosing to evaluate total transport through a wider Barents Sea Opening section (Figure 1). This can be justified because the short AW section in the model may not fully capture the location of AW inflow in the simulation. The wider section (blue line; average 2.3 Sv) is in better agreement with the observed mean 2.3 Sv of net transport through the Barents Sea Opening. The difference in interannual

variability between the simulated and observed transport could also be partly due to the processing and extrapolation of mooring observations that have both spatial and temporal gaps (Ingvaldsen et al., 2004a). The amplitude of interannual variability (12-month running mean) in the model and observations are 0.27 and 0.4 Sv respectively. The amplitude of the seasonal climatology in the model and observations are 0.60 and 0.28 Sv respectively. The observed time series exhibits more high frequency variations than the simulated one (Figure 3a), which could be the signature of mesoscale eddies passing through the section that the model cannot resolve. Overall, the model has been shown to simulate the important features and thus can be used to investigate the processes giving rise to variability in watermass properties.

3. Quantifying Variability in BSW Properties

To investigate the drivers of the seasonal to interannual variability in AW and BSW volume in the central Barents Sea, we evaluate the volume, heat and freshwater budgets within the central Barents Sea. The positions of the boundaries of the selected box in the Barents Sea roughly encompasses the region where AW and BSW are expected to be in contact with the atmosphere or sea ice during winter (Figure 1). The boundaries of this box are simplified into four parts (North, East, South, and West) as shown by the different colors on the map. The main contribution to the total inflow to the box is through the West boundary (i.e., AW inflow), while BSW represents the bulk part of the outflow, and the larger outflow from the box is through the East boundary toward the Kara Sea and the St. Anna Trough. The transports through the South and North boundaries are very small in comparison to the West and East boundaries. The South boundary largely corresponds to the Coastal Front and land boundary, while the North boundary is roughly aligned with the Polar Front across which the advection is negligible.

3.1. Watermass Volume and Properties

We start by examining the variability in volume and properties of the different watermasses found within the Barents Sea.

We calculated the volumes of the watermasses by integrating the volume of grid cells matching the respective properties of the different watermasses (Table 1) within our box. This is also given as a percentage of the total volume of the budget box for each watermass. BSW makes up the largest watermass by volume, followed by AW and finally ArW (Figure 5a). The amplitude of the simulated seasonal cycle in BSW volume is 0.16×10^{14} m^3, while the seasonal amplitude in AW volume is 0.11×10^{14} m^3. The seasonal cycles of AW and BSW are in opposite phase that is, when BSW volume increases in winter, AW volume decreases (Figure 5a). This reflects the winter transformation of AW into BSW at the seasonal time-scale and subsequent summer replenishment of the pool of AW.

When we averaged over our 30-year long simulation, the mean BSW volume occupies 48% of the budget box (0.76×10^{14} m^3) and the amplitude of interannual variability is 0.13×10^{14} m^3. The time series of BSW volume exhibits two large minima, one where BSW occupies <30% of the budget box at the seasonal time scale (0.5×10^{14} m^3) in 1990 and one where is fills only <25% of box (0.4×10^{14} m^3) in 2004. In 1990, the minimum in BSW volume is preceded by a peak in ArW volume where it fills 8% of the budget box (0.1×10^{14} m^3) and the 2004 minimum in BSW is preceded by an ArW volume peak filling 15% of the budget box (0.3×10^{14} m^3). In both cases, 2 years after the ArW volume peak, AW volume increases from filling around 20% of the budget box (0.3×10^{14} m^3) to 35% of the budget box (0.6×10^{14} m^3), compensating the minimum in BSW volume. Compared to the amplitude of the interannual variations, these anomalies are noteworthy and will be addressed in greater detail in Section 4. Notice that part of the interannual variations in BSW volume results from a seasonal imbalance between formation and export, as a portion of the BSW volume is exported from the formation region every year but a reservoir remains (Figure 5). The reservoir enables watermass properties to persist from 1 year to the next, representing the "memory" of this system. This is important because these persistent properties ultimately influence the properties of the BSW exported to the Arctic, and thus the properties of the Arctic Intermediate Water. The minima events in BSW volume are of particular interest because they mark occasions where larger differences in historic BSW properties can manifest.

Interannual variability in watermass volumes are associated with changes in temperatures and salinity, as shown in Figure 6. This figure shows the temporal and depth distribution of temperature, salinity and density anomalies in the color shading with the volume of each watermass, AW, ArW, and BSW superimposed as dashed lines on

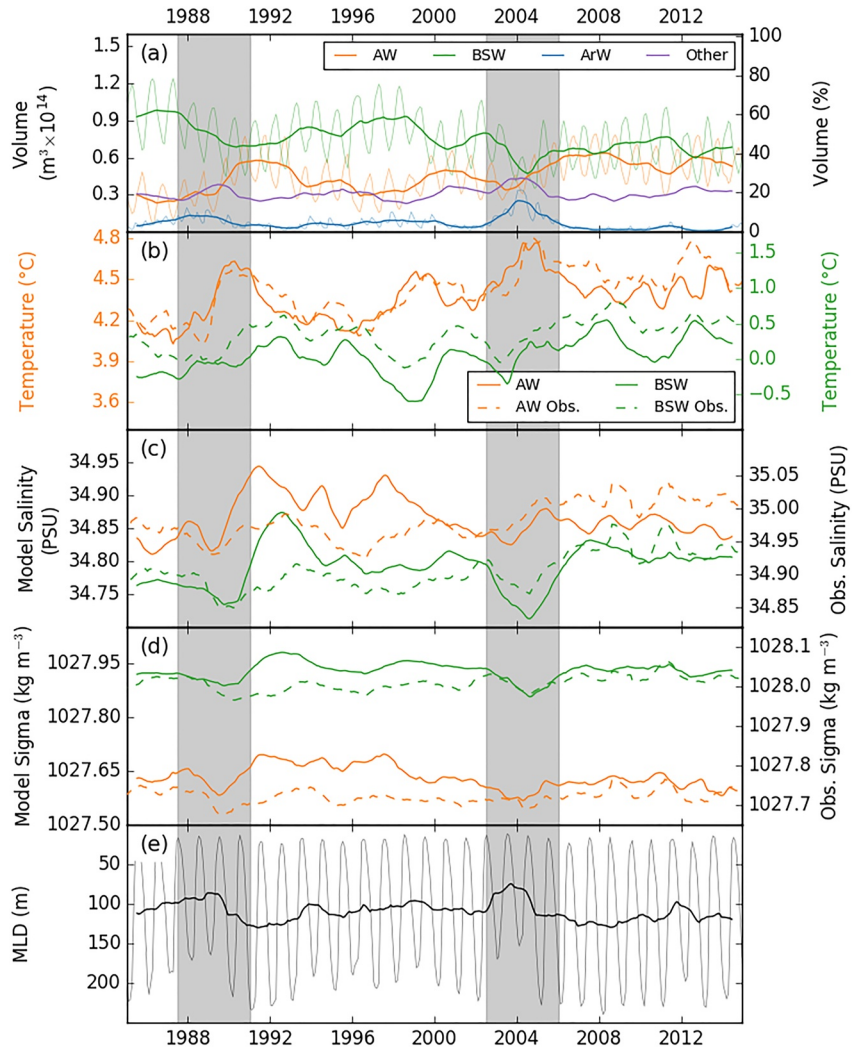

Figure 5. Properties within the budget box shown in Figure 1. In each panel the different watermasses are represented by the color in the legend with solid lines showing model values and dashed lines showing observation from the EN4 data set. Thin line show monthly data and thick lines show 12-month running means. The other category in (a) shows the volume of other watermasses not included in our analysis. (a) The watermass volumes (percentage of the budget box filled on right axis), (b) temperature (where Atlantic Water is on left axis, Barents Sea Water is on right axis), (c) salinity (where model is on left axis, EN4 is on right axis), (d) density (where model is on left axis, EN4 is on right axis) and (e) the model mixed layer depth in black. The gray bars highlight periods of interest July 1987 to December 1991 and July 2002 to December 2005 events.

top of each panel respectively. Within the water column, temperature anomalies are associated with AW volume anomalies, the freshest salinity anomalies are associated with ArW volume anomalies, and density anomalies are associated with BSW volume anomalies, as would be expected from the T-S diagram in Figure 2. AW temperature is correlated with AW volume (r-value = 0.78, lag = 20 months, where AW temperature leads). Minima in BSW volume anomalies follow minima in salinity anomalies and roughly coincide with warm temperature anomalies. BSW salinity is correlated with AW salinity (r-value = 0.66, lag = 13 months, where AW leads), and BSW salinity is correlated with net sea ice melt (r-value = −0.7, lag = 13 months, where melt leads). As a result, AW temperature is correlated with BSW salinity (r-value = 0.54, lag = 31 months, where AW leads). This correlation is in agreement with model results reported by Årthun et al. (2011) and Oziel et al. (2016). The salinity and density anomalies appear first at the surface and propagate downwards through the water column in 1–2 years, as revealed by the Hovmöller plots shown on Figure 6. In contrast, with the exception of 2004, the temperature anomalies do not show a similar downward propagation through the water column and tend to be present throughout the water column at once. This indicates that subsurface temperature anomalies are largely advected

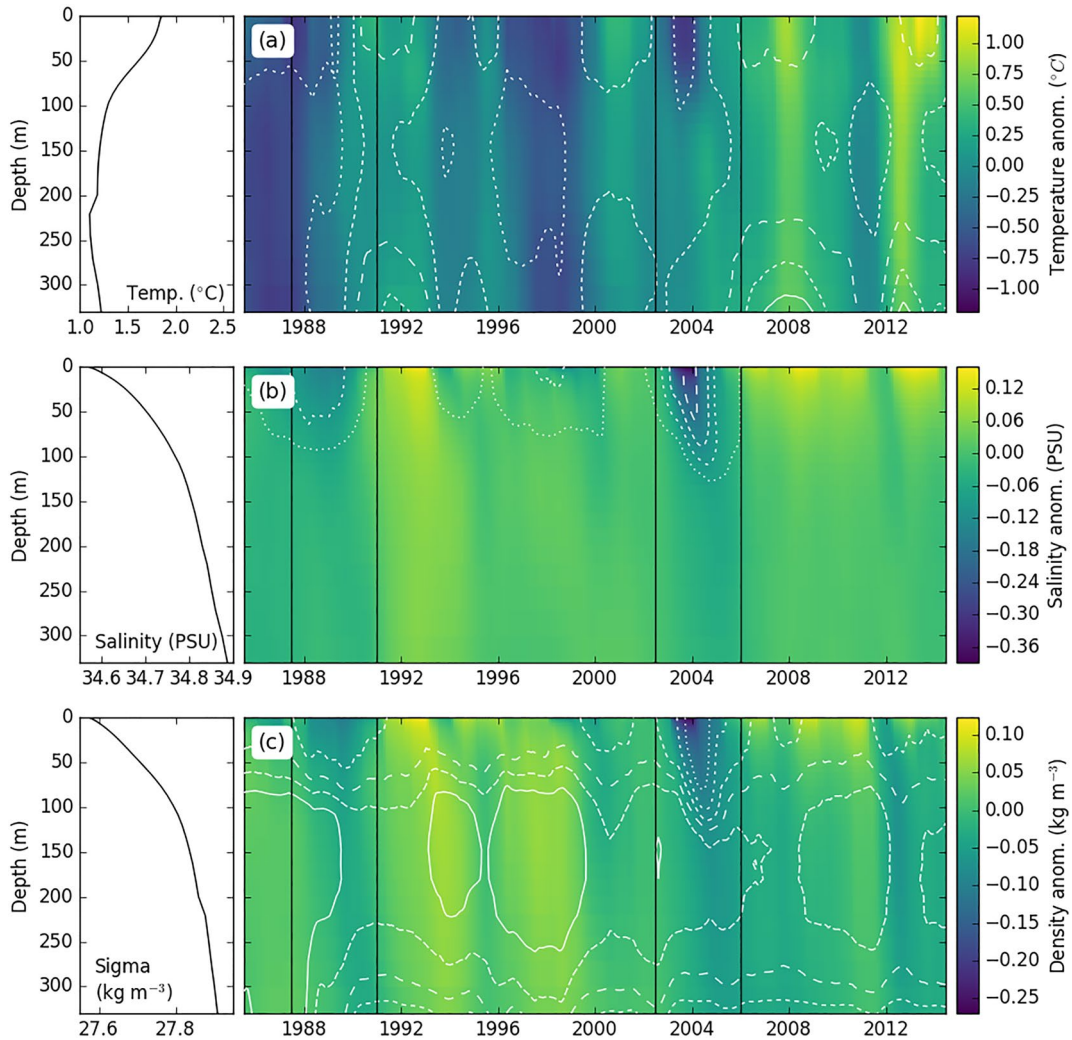

Figure 6. Hovmöller plot showing interannual variability anomalies for (a) temperature, (b) salinity and (c) density averaged with the box shown in Figure 1. The anomalies are calculated by subtracting the time-averaged T, S or density profile (shown in the panels left of (a–c)) from the respective 12-month running mean profile to focus on interannual variability. The contour lines show the percentage of the water column within the box occupied by (a) Atlantic Water, (b) Arctic Water, and (c) Barents Sea Water, again with a 12-month running mean. Contour lines at 10% intervals from 10% (dotted line) to 60% (solid line) with lines becoming more solid with increasing percentage of the box that is filled by the respective watermass. Note the depths below 300 m are only present in the western Barents Sea. Solid black vertical lines highlight periods of interest July 1987 to December 1991 and July 2002 to December 2005 events.

into the box rather than surface forced. Surface temperature minima (likely forced by the atmosphere) are visible in 1989, 1997, and 2003 but these anomalies remain confined to the surface layer. The surface temperature minimum in 2003 (when ArW is present) is −0.75°C compared to the mean temperature profile, which shows a surface-to-bottom temperature difference of 0.6°C (left panel in Figure 6a). This cold water at the surface means the water column does not have a strong vertical temperature gradient and the salinity gradient is strong.

The difference between the simulated and observed AW salinity is −0.1 PSU making it fresher on average, but this varies between −0.02 and −0.15 PSU (Figure 5c). This suggests that the model overestimates a source of freshwater in the inflowing AW during this period. The narrow Norwegian coastal current (which carries waters fresher than AW) is poorly captured by the model and may be mixing more with AW than in observations. Coastal currents are a common deficiency in numerical models even at high resolution (e.g., Wekerle et al., 2017). The fresher model may artificially shallow the mixed layer depth in the model, particularly during periods with the largest difference, given that the model shows mean AW salinity is correlated with mixed layer

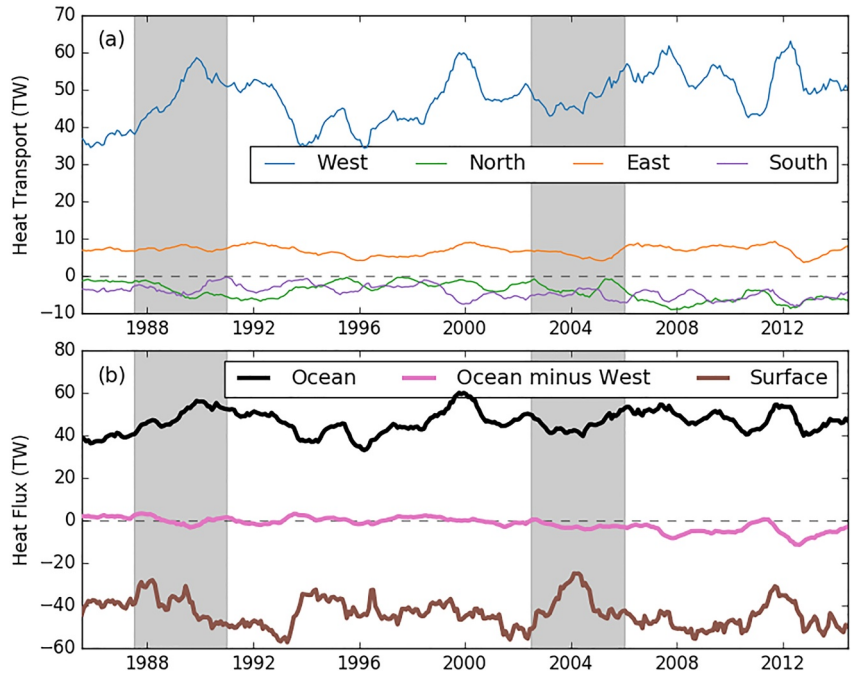

Figure 7. Heat budget within the budget box. All time series have been smoothed with a 12-month running mean. Positive values indicate flux into the box. (a) Ocean heat transport at the West, North, East, and South boundaries for the box shown in Figure 1. In each panel the color of the line corresponds to the color of the boundary on the map. (b) The black line is the total sum of ocean heat transport in (a). The pink line is the sum of ocean heat transport from only the North, East and South boundaries that shows heat is exported through these boundaries later in the time series. The brown line is the net surface heat flux integrated over the surface area of the box in Figure 5 (a negative value represents a heat flux upward from the ocean to the atmosphere). The gray bars highlight periods of interest July 1987 to December 1991 and July 2002 to December 2005 events.

depth (r-value = 0.4, lag = 2 months, where AW leads). There are fewer salinity measurements in the EN4 data than temperature measurements, suggesting the smaller variability in observed salinity may be the result of spatial and temporal interpolation smoothing the intensity of peaks between the sparse observation profiles. The observations also tend to be biased toward the more saline southwestern Barents Sea. Figure 5 shows that the change in salinity when AW forms BSW is 0.07 PSU for both the model and the observations, suggesting that the simulation adequately captures the processes at play for the formation of BSW. Similarly, the density change from AW to BSW is 0.30 and 0.28 kg m^{-3} for the model and observations, respectively, reinforcing the idea that BSW salinity variability is primarily set by AW salinity variability, providing justification for the choice to adjust the watermass definitions for the model (Table 1).

From 2004 up to the end of the model run, AW volume and temperature inside the box increases, as does BSW temperature (Figure 5b). The increase in AW volume is in agreement with the results of Oziel et al. (2016), who also reported that the southern thermal front (between AW and BSW) moved eastwards during 1998–2000. Similarly, over that period, we see an increase in AW volume that could be attributed to this front movement (Figure 5a). After 2004, there is stronger surface heat flux than before 2005, and sea ice extent and net melt tends to decrease and be less variable (Figures 3, 7b, and 8b).

3.2. Heat, Freshwater and Watermass Transport Budget

When we computed the volume transport across the different sections closing our box, we found an average transport of 2.1 Sv into the box, that comes almost entirely through the Barents Sea Opening at the West boundary, while 1.53 Sv exits through the East boundary (Figure 1). As expected, this budget is closed by smaller mean transports out of the box through the North and South boundaries of 0.26 and 0.34 Sv respectively. The West and East boundaries lie across the path of AW and BSW as these watermasses transit through the Barents Sea. Next

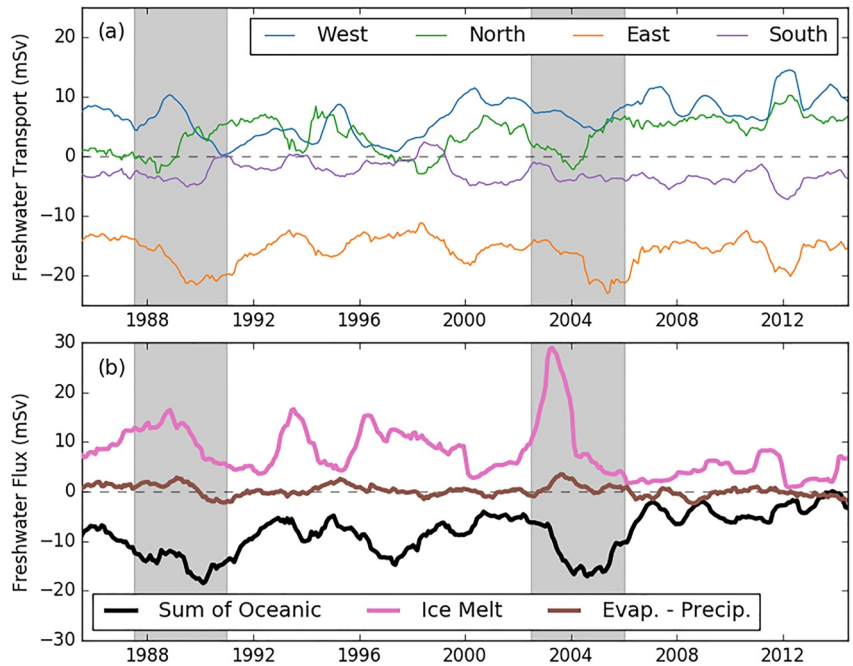

Figure 8. Freshwater budget within the budget box. All time series have been smoothed with a 12-month running mean. Positive values indicate flux into the box. (a) Ocean freshwater transports across the West, North, East, and South boundaries of the box shown in Figure 1. In each panel the color of the line corresponds to the color of the boundary on the map. (b) The black line is the total sum of ocean freshwater transports in (a). The pink line is the net sea ice freshwater flux (melt—freeze) integrated over the surface area of the budget box (not white line) in Figure 1 (positive values show freshwater flux into ocean). The brown line is the net evaporation–precipitation (E–P) where positive values indicate net freshwater flux into the ocean. The gray bars highlight periods of interest July 1987 to December 1991 and July 2002 to December 2005 events.

we evaluate the different terms of the heat and freshwater budgets (Equations 1 and 2) in order to better understand the drivers of the watermass variability.

Average heat transport entering our box through the West boundary is 47 TW, within the range of observed heat transport of 49 TW ±7 TW (Skagseth, 2008) and previous model estimates (71 TW in Smedsrud et al. (2010) and 28 TW in Årthun and Schrum (2010)). This heat inflow is augmented by an apparent heat input (technically from an outflow of waters with negative temperatures) of 6.9 TW at the East boundary (in agreements with estimates from Schauer et al. (2002), Gammelsrød et al. (2009) based on observations) and export of 4.1 and 4.3 TW at North and South boundaries (Figure 7a). The bulk of the heat (Q_{adv}) entering through the West boundary is lost to the atmosphere within the box, with an average integrated surface heat flux (Q_{surf}) of 45 TW (Figure 7b). This is again consistent with the model analysis of Årthun and Schrum (2010) who estimated an integrated surface heat flux of 40 TW.

The heat transport through the West boundary exhibits variability on both seasonal and interannual time-scales (with respective amplitude of 16.6 and 6.8 TW; Figure 7). Unsurprisingly, the variability in integrated surface heat flux is dominated by a seasonal cycle with amplitude reaching 86 TW, driven by seasonal solar heating. The amplitude of both interannual and seasonal variations at the other boundaries are all less than 5 TW (Figure 7a). From 2003 onward, the heat transport through the West boundary falls out of balance with the heat export through the surface (pink line, Figure 7b). This results in an increasing amount of heat being exported through the South, East and North boundaries. This amounts to a divergence of 5–10 TW by 2012. This imbalance will also contribute to changing watermass temperatures (heat storage) in the budget box. This agrees with other results that more oceanic heat is leaving the Barents Sea to the north and the cooling through air-sea fluxes here no longer keeps pace with the warming AW (Skagseth et al., 2020).

The mean freshwater transports at the West and North boundaries are 6.8 and 3.7 mSv respectively (Figure 8a). Smedsrud et al. (2010) estimated the freshwater transport of the Norwegian Coastal Current as 20 mSv, which is greater than our freshwater transport through the full West boundary. However, our box does not fully account

for the Norwegian Coast Current, in contrast to the region considered by Smedsrud et al. (2010) (Figure 1). The East and South boundaries have mean freshwater export of 15.9 and 2.9 mSv respectively (Figure 8a). The sum of the freshwater transport (F_{adv}) across the four sections is −8.0 mSv on average, and can reach beyond −15 mSv for example, in 1990 and in 2004. This imbalance is compensated by the freshwater fluxes at the surface (F_{surf}) (including net sea ice melt) and change in mean salinity within the box (freshwater storage): there are no river sources because the box does not boarder land.

On average, precipitation and evaporation roughly offset each other, with a small mean residual of 0.14 mSv (0.02 mm day^{-1}) of freshwater input into the ocean. This mean atmospheric freshwater flux is not enough to balance the net freshwater transport budget (Figure 8b), and the contribution coming from sea ice processes (resulting from melting and freezing) must be considered to close the budget. We calculated sea ice freshwater flux over the area of the budget box (Figure 1). The sea ice freshwater flux has a mean value of 8 mSv, balancing the oceanic net freshwater transport out of the box (Figure 8b). This term is almost always positive (Figure 8b). In addition, Figure 9e shows the sea ice volume transport across the boundaries of the budget box showing that there is net sea ice import to the domain across the North boundary (in agreement with Lind et al. (2018)). The strong net sea ice import and net melting versus freezing within the budget box show the sea ice is a source of freshwater. The sea ice freshwater flux into the budget box is dependent on sea ice import. Sea ice extent is correlated with AW temperature (r-value = −0.61, lag = 23 months, where AW leads) and net sea ice melt is correlated with AW temperature (r-value = −0.57, lag = 19 months, where AW leads). After 2005, sea ice extent and import is reduced (Figure 9e), consistent with the regime shift discussed by Barton et al. (2018). Net sea ice melt flux has a mean of 10 mSv for 1985–2005 and 4 mSv for 2005–2015.

In addition to the full heat and freshwater budgets performed for the full box, we also estimated the closed watermass volume budget (see Equation 3) in order to gain some understanding of the changes in the volume occupied by the different watermasses. Figure 9 shows the advection ($\Delta\Psi_{adv}$) of AW has a large import of 2.03 and 0.17 Sv is exported, leaving mean net import of 1.86 Sv. Advection of BSW has net mean export of 1.66 Sv; 1.12 Sv of this occurs through the East boundary and the rest is exported through North and South boundaries. Advection of ArW has 0.23 Sv of import through the North boundary, however, 0.41 Sv of ArW is exported through the East boundary and an additional 0.09 Sv is exported at the South boundary. The black line on Figure 9c shows the mean net ArW export is 0.26 Sv. The total volume transport of other watermasses that do not fit the three main watermass categories is shown in Figure 9d to roughly close the budget. The other watermasses are largely made up of Coastal Water and the seasonal surface mixed layer water which tend to be warm and fresh. The mean net transport of other watermasses is −0.03 Sv. Sea ice volume contributes a net mean 0.01 Sv import and evaporation minus precipitation is 0.14 mSv making surface volume flux (Ψ_{surf}) mostly negligible to the volume changes. We solved Equation 3 for the watermass transformation M and neglected the surface volume fluxes (Figure 10). The watermass transformation in Figure 10 confirms our earlier statements that AW transforms into BSW and a small portion of ArW.

ArW export becomes balanced by ArW import between 2006 and 2015 (Figure 9e). During this time sea ice import and net melt also reduces. This shows that the net sea ice melt is a main freshwater source for ArW formation in the budget box and formation of ArW largely stops after 2006 (Figure 10). BSW export and formation is greater in 2006–2015 than 1985–2006 while ArW export is smaller in 2006–2015 than 1985–2006 (Figure 9). This suggests that during the earlier period, AW (or BSW) mixes with freshwater in the surface layer released by the net sea ice melt to form ArW. The ArW produced in this way would have contributed to the net ArW export in 1985–2006 and the loss of net sea ice melt stops this source of ArW formation after 2006. This may have contributed to the warming and increasing salinity of the ArW in the northern Barents Sea discussed by Lind et al. (2018).

To summarize, the timing of the seasonal cycle in BSW volume has the opposite phase to the AW volume (Figure 5a), resulting from seasonal transformation of AW into BSW. This seasonality in volume in combination with the net BSW export (Figure 9b) shows that some BSW is removed from the box but the remaining volume gives it a "memory" of the previous year's properties. In two instances, in 1990 and 2004, the volume reaches minima, and the "memory" is thus reduced. Between 1985 and 2003 the ocean heat transport is roughly balancing the surface heat flux (Figure 7b). However, after 2003 the West boundary heat transport is no longer balanced by atmospheric heat flux (Figure 7b), reflecting a warming of the watermasses found within the Barents Sea. From the watermass budget, we know AW is mostly imported and that it is largely transformed into BSW, the main

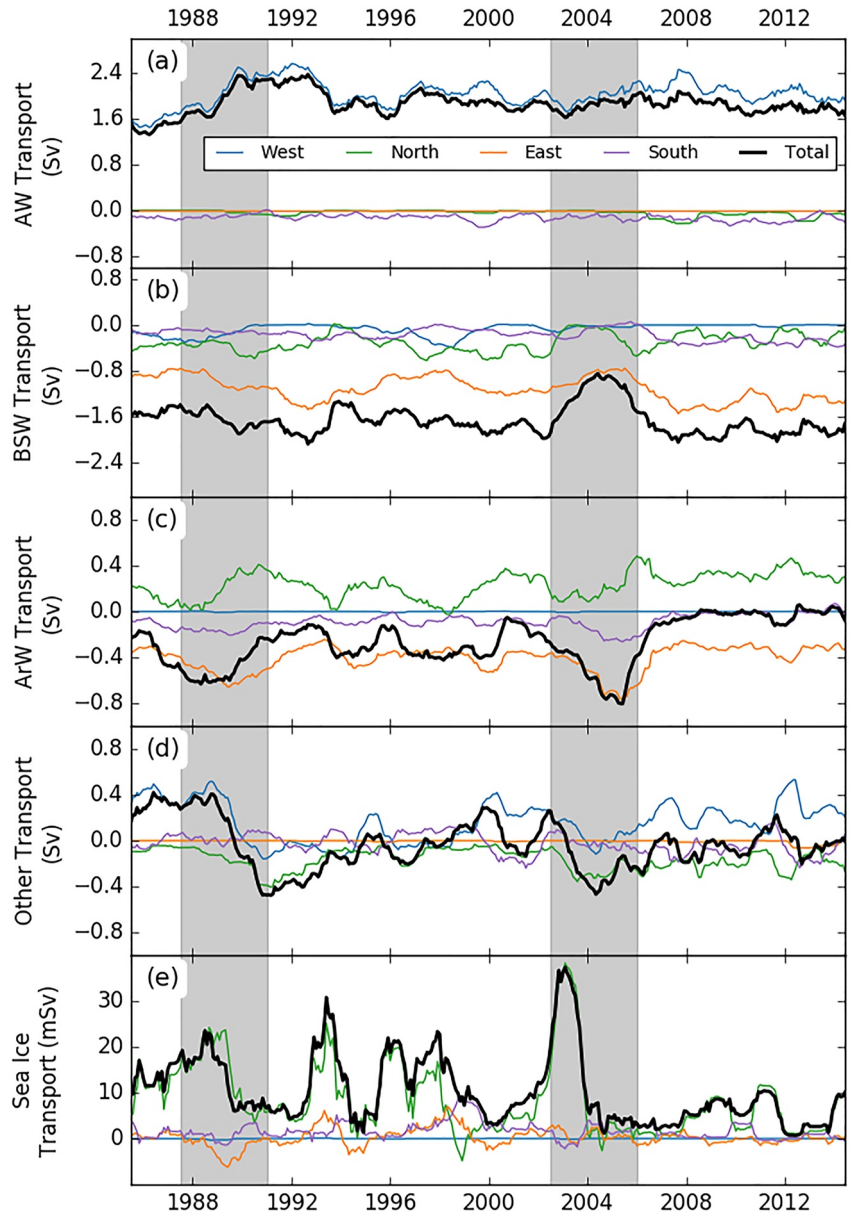

Figure 9. Watermass transport budget within the budget box. All time series have been smoothed with a 12-month running mean. Positive values indicate flux into the box. Transports are across the West, North, East and South boundaries of the box shown in Figure 1 with the color of the line corresponding to the color of the boundary on the map. The black line is the total sum of the respective watermass transports into the budget box. (a) Atlantic Water (AW) transport, (b) Barents Sea Water (BSW) transport, (c) Arctic Water (ArW) transport, (d) other watermasses not included in AW, BSW or ArW definitions (see Table 1) and is mostly composed of coastal water and surface mixed water, (e) sea ice and snow transport into the budget box. The gray bars highlight periods of interest July 1987 to December 1991 and July 2002 to December 2005 events.

export (Figure 10). Some AW is also transformed into ArW in combination with freshwater sourced from the net sea ice import.

4. BSW Minimum Events

Throughout the simulation, we can identify several extrema of BSW properties. These events are most pronounced in the volume and salinity minima of BSW that occur in July 1987 to December 1991 and July 2002 to December 2005 (Figure 5). While the 1987–1991 event is less pronounced, it gives context to the 2002–2005 event. These

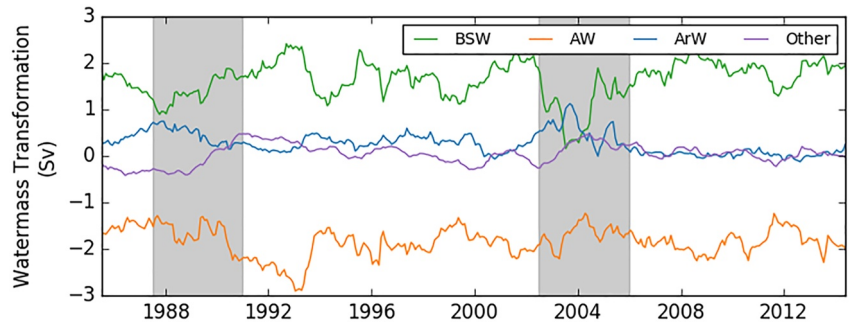

Figure 10. Watermass transformation within the budget box calculated from watermass volume change and watermass transport. All time series have been smoothed with a 12-month running mean. Positive values indicate flux into the box. The gray bars highlight periods of interest July 1987 to December 1991 and July 2002 to December 2005 events.

two events are the focus of this section because they represent times when there is a smaller reservoir of BSW and a reduced "memory" of BSW properties within the box. A smaller reservoir means less stability in BSW properties because the annual formation of new BSW that is mixed into the reservoir of older BSW will have greater potential to dilute the reservoir and modify the properties of the watermass stored in the reservoir.

Focusing first on the period 1987–1991, the fractional volume of BSW filling the budget box reduces from 60% to 40% (1.0×10^{14} m^3 to 0.7×10^{14} m^3) and is accompanied by a decrease in BSW density, mainly due to a freshening (Figure 5). Before this event, in 1989, the sea ice extent is relatively large, reaching 1.1×10^{12} m^2. The event is triggered by the low temperature of the AW in the late 1980s and the import of sea ice producing a source

Table 2
Table With a Description of the Evolution of Properties Over the 1987–1991 Event and 2002–2005 Event

1987–1991 Event	Evolution	2002–2006 Event	Figure
*Cool AW temperature	**Stage 1**	*Cool AW temperature	5b
*Winter Sea ice expansion and import	↓	*Winter sea ice expansion and **extensive** import	3c, 9e
*Warming AW temperature	**Stage 2**	*Warming AW temperature	5b
Large summer net sea ice melt	↓	**Very** large summer net sea ice melt	8b
	↓	**Strong vertical salinity gradient**	5e and 6b, 6c
Freshwater exported in ArW	↓	Freshwater increases ArW **volume** and export	5a, 9c
Some freshwater reduces BSW salinity	↓	Some freshwater reduces BSW salinity	5c
Surface heat flux **increases due to AW temperature**	↓	Surface heat flux **decreases due to insulation**	7b, 6a
BSW formation decreases BSW export **maintained**	↓	BSW formation and export **decreases**	9b, 10
BSW volume minima AW volume increases	↓	BSW volume minimaAW volume increase	5a
*Sea ice net import reduces	**Stage 3**	*Sea ice net import reduces	9e
BSW salinity no longersuppressed by net sea ice melt	↓	BSW salinity no longersuppressed by net sea ice melt	8b, 5c
BSW formation increases	↓	BSW formation and **export** increases	5a, 9b, and 10
AW volume **decrease** BSW volume **restores** ArW net export **reduces**	**Stage 4**	AW volume **maintained** BSW volume **not fully restored** ArW net export **stops**	9a–9c

Note. Stages extend downwards until a new stage is reached showing key changes that occur during the event. The stages are consecutive over the event. * indicates external forcing to the budget box. Bold text highlights the differences between events.

of freshwater from melting (Stage 1 in Table 2). The sea ice extent decreases to 0.9×10^{12} m^2 during the event as AW warms (Figure 3). The balance of ice freezing/import is outweighed by local melt and this contributes to freshening of BSW (Stage 2 in Table 2). The 1987–1991 freshwater anomaly is due to 15.0 mSv net sea ice melt in 1987–1990, together with the small net freshwater input from net precipitation of 1.5 mSv in 1989, and decreasing net ArW export during 1989–1990 (Figures 8b and 9c). The greater freshwater content adds buoyancy to the upper ocean, resulting in a shoaling of the winter mixed layer from 200 m in 1986 to 160 m in 1989 (Figure 5). The input of freshwater and increase in ArW volume strengthens the water column density gradient before the freshwater anomaly is mixed downwards and exported through the East and North boundaries as ArW and relatively low salinity BSW (Figure 6).

Between 1989 and 1990, AW temperature also increases, followed by the larger surface heat lost to the atmosphere found in the period considered (Figures 5 and 7b, Stage 2 in Table 2). Volume and heat transports through the West boundary also reach local maxima of 2.5 Sv and 60 TW respectively (Figure 7a). In this case, the increase in heat transport leads the surface heat flux, suggesting that it is driving an increase in surface heat flux. This interpretation is contrary to the more commonly accepted view that the atmosphere forces the ocean (Blackport et al., 2019). Here, the Barents Sea ocean temperature anomalies do not begin at the surface but appear throughout the water column simultaneously (Figure 6), in agreement with the findings of Schlichtholz (2019). If the atmospheric heat divergence were driving the ocean heat convergence the mean ocean temperature should decline. However, our results show the ocean temperature increases (Figure 5b) and our heat flux budget in Figure 7b shows depth integrated ocean heat convergence is balanced by atmospheric heat divergence.

The positive ocean temperature anomaly shown in Figure 6 contributes to increasing the AW volume that replaces BSW, resulting in the BSW volume minima around 1990 (Figure 5a, Stage 2 in Table 2). Figure 9 shows increasing AW import during the 1987–1991 event. This is paired with maintained BSW export, though this does not compensate for the increase in AW volume inflow, showing overall a reduction in the transformation of AW to BSW (Figure 10). There is also decreasing ArW export and increasing export of other watermasses. Since transformation of AW to BSW slows and AW import remains, the volume occupied by AW increases. As the event evolves through 1991–1992, salinity and density of BSW increase due to the reduced freshwater flux from receding sea ice and reduced sea ice import (Stage 3 in Table 2). At this point inflowing AW salinity variability becomes larger and the salinity of BSW increases (Figure 5c). As the properties return to values before 1987, the formation, export and volume of BSW increases (Stage 4 in Table 2). The salinity increase also drives a decrease in the upper ocean buoyancy (positive density anomaly in upper 50 m in 1991–1992) and a deepening of the winter mixed layer down to 230 m in 1991 (Figures 5 and 6). The salinity increase in AW and BSW following 1991 can also be seen in observations. Although the 1992 peak in AW salinity is not present in the observations, BSW salinity closely follows AW salinity to a smaller peak, once the sea ice freshwater flux is reduced. As mentioned in Section 3, a variable salinity bias exists between the model and observations. Though the intensity of the salinity anomaly is smaller in observations, it still occurs and does not affect our conclusions.

We now focus on the 2002–2005 BSW volume minimum event, during which BSW density and salinity also exhibit marked minima (Figure 5). The evolution of properties during this event is summarized in Table 2 for comparison with the 1987–1991 event. In the 2002–2005 event the BSW volume occupying the budget box reduces from 50% to 30% (0.75×10^{14} m^3 to 0.45×10^{14} m^3). It occurs at the same time as a marked increase in ArW volume, filling 15% of the budget box (3.5×10^{13} m^3) (Figure 5a). The density and volume minima are also the result of fresher and warmer BSW. The trigger for the 2002–2005 event is the sea ice import anomaly, which also coincides with the cool AW temperature anomaly in 2001 (Stage 1 in Table 2). Similar to the 1987–1991 event, sea ice extent is higher than average in winter 2003 (Figure 3) but, unlike the 1987–1991 event, this is followed by an exceptionally large peak in sea ice import in winter 2002–2003 (Figure 9e) and subsequent net sea ice melt of 28 mSv in summer 2003 (Figure 8b, Stage 2 in Table 2). The ArW import is relatively low so that the ArW volume peak is locally produced by mixing of AW (or BSW) with freshwater resulting from the net sea ice melt. This anomalous freshwater input also causes the BSW salinity minimum in 2004 (Figure 6b). BSW export is reduced to 0.8 Sv in 2004 from 1.6 Sv in 2002 showing BSW formation is again slowed but more substantially than the 1987–1991 event, with formation reaching <0.5 Sv in 2003 (Figure 10). ArW export increases to 0.8 Sv in 2005 from 0.3 Sv in 2002 while ArW formation is greater. Transport of other watermasses also switches from import to export during this event due to a minor increase in formation.

Unlike the 1987–1991 event, the volume and heat transports though the West boundary remain relatively small in 2004 (1.9 Sv and 40 TW; Figure 7a). The surface heat flux also remains smaller than during the 1987–1991 event, only reaching 24 TW, which at the interannual time scale does not balance the 40 TW net heat transport anomaly (Figure 7, Stage 2 in Table 2). The combined effects of this imbalance in heat fluxes (which tends to isolate warm water below the surface at 150 m in 2005; Figure 6) results in a warm BSW temperature anomaly into 2004 and beyond. In contrast to 1987–1991, the decrease in surface heat flux is the result of the temporary fresher surface layer formed within the box, limiting the average winter mixed layer depth to 150 m in 2004 (Figures 5 and 6). The main difference between 1987–1991 and 2002–2005 for surface heat flux is that, the vertical ocean temperature gradient is weak and the vertical salinity gradient is strong during 2002–2005 and the mixed layer depth increases, so AW heat loss to the atmosphere is more limited (Figures 5e and 6). This reduces the transformation rate of AW into BSW in 2002–2005, and the resulting BSW is cooler than in previous years (Figure 10). The decrease in winter mixed layer depth in 1988 appears to have the same effect, decreasing surface heat flux, albeit to a lesser extent. In 2005, the sea ice import and net melt has reduced (Stage 3 in Table 2). The transformation of AW to BSW does not increase sufficiently in 2005–2015 and only restores BSW volume to 44% of the budget box (Stage 4 in Table 2). Net formation of ArW within the budget box is eliminated after 2006 following the loss of sea ice import. In agreement with this, after 2005, positive density anomalies appear near the surface that tend to weaken the water column stability and deepen the mixed layer depth (Figure 6). The 2004 BSW minimum event is of interest because of the shift in Barents Sea properties that follows. Next we summarize and discuss these changes.

5. Discussion

Based on our understanding of the two events in 1987–1991 and 2002–2005, we now discuss the mechanism that would cause a regime change, like 2002–2005, to occur following a hypothetical trigger in the future. Climate projections from an ensemble of models show there is a 40% possibility that lost winter sea ice in the south-eastern Barents Sea could begin to re-expand by 2040, reversing the trend from the decline that occurred between 2000 and 2015, but additional decline is likely (Årthun et al., 2019). By understanding the ocean variability surrounding 2005, we can identify the conditions that would produce another step change following a hypothetical trigger. The sequence of events leading up to the shift in regime in 2002–2005 was as follows:

1. A long-term trend in increasing AW temperature warms the western Barents Sea from 2000 onward (Levitus et al., 2009; Lind et al., 2018).
2. In 2002–2003 there is anomalously large winter sea ice extent and import leading to an unusually large net sea ice melt in summer 2003.
3. The freshwater released by net sea ice melt decreases upper salinity and density, while mixed layer depth increases and thus decreases the formation of new BSW, reducing the volume and export of BSW in 2004.
4. Once this fresher, more buoyant BSW and ArW water is advected out of the eastern Barents Sea, a greater volume of warmer AW occupies the Barents Sea after 2005.
5. The long term trend of warming AW (Levitus et al., 2009; Lind et al., 2018), maintains the loss in sea ice extent after the large net melt in 2003.

This sequence of events shows that, with the reduced net sea ice melt after 2005 (purple line, Figure 8b) and the reduced strength and variability in density anomalies (Figure 6c), AW temperature is able to have a greater influence on the surface heat flux and oceanic heat exported from the region. Our analysis shows rising AW temperature is the key factor in preventing a return to the regime before 2002. If a cold anomaly in AW temperature were to be advected into the Barents Sea, this would tend to result in a reverse regime shift toward conditions that are seen before 2002. This could not be initiated by sea ice import since this would produce a complementary freshwater event.

The analysis suggests a second complementary regime change could occur in the future, on the condition that AW temperature continues to increase the overall temperature of the Barents Sea. The increasing heat transport through the Barents Sea Exit (BSX in Figure 1) suggests the temperature trend is already propagating further north, and larger regions of winter sea ice loss could occur, as supported by the results of Lind et al. (2018), Årthun et al. (2019), and Lique et al. (2018). As the event in 2002–2005 has a positive freshwater anomaly from net sea ice melt, our analysis shows that a freshwater anomaly would also be needed to reduce the formation and volume of BSW in the area, before a further step change could occur. It has been noted that a large fresh anomaly observed in the Atlantic Ocean, is heading for the Barents Sea and could contribute to a future disruption of BSW formation (Holliday et al., 2020; Skagseth et al., 2020).

6. Conclusion

The Barents Sea has seen significant changes in sea ice and watermass properties around the mid-2000s (Årthun et al., 2012; Barton et al., 2018; Herbaut et al., 2015; Lind et al., 2018). Using a high-resolution ocean-sea ice model of the Arctic Basin, we have investigated the interannual variability in a box encompassing the southern Barents Sea largely occupied by AW and BSW. The simulation is validated with satellite SST fronts, sea ice, AW transport and hydrographic profiles. The heat budget shows heat transport through the Barents Sea Opening is almost entirely balanced by surface heat loss. The freshwater budget reveals that freshwater export through the Barents Sea Exit is a product of freshwater import from the Barents Sea Opening and sea ice processes. Variability in these processes alter the volume of BSW formed each year, affecting the stability and "memory" of the previous years properties. BSW volume variability exhibited two anomalously low events in 1987–1991 and 2002–2005. Comparison of the two anomalies reveals a similar sequence of events leading to the anomalies where there is period of larger winter sea ice extent and subsequently larger summer net sea ice melt. This freshwater release combined with relatively fresh AW caused the BSW volume minima that was subsequently filled by expanding AW volume. The fresh meltwater release in the 2002–2005 event is more extreme than the 1987–1991 event as a result of sea ice import, this reduces the formation and volume of BSW in the box. Net ArW formation within the box also stop after 2006. The BSW formation stabilizes at a new equilibrium where there is a greater volume of warmer AW present, completing the regime change.

If recent trends continue, it has also been suggested that the Atlantification of the Barents Sea could extend beyond the Barents Sea into the Eurasian Basin, deepening convection there (Lique et al., 2018). Through long term variability, sea ice has a chance of returning to pre-2002 conditions in the 2040s (Årthun et al., 2019). Our results suggest a reversal in the sea ice regime change would be unlikely given the reduced volume "memory" of those conditions in BSW. This is important for sea ice prediction attempts such as Onarheim et al. (2015) because the sea ice extent in the northern Barents Sea is correlated with AW and ArW temperature even after the regime change (Lind et al., 2018). Understanding the Barents Sea temperature and heat flux variability under the present regime is also important for the coincident extreme weather events in Europe and Asia (Blackport et al., 2019; Hoshi et al., 2019; Luo et al., 2016; Petoukhov & Semenov, 2010).

Data Availability Statement

Version 1.1 of the CREG12. L75-REF08 Canadian Regional model based on NEMO used for producing the model output is preserved at https://doi.org/10.5281/zenodo.5789520, available via Open access without registration. This documentation includes links to boundary forcing, atmospheric forcing and initialization files. Version 3.0.2 of the CDFTOOLS software used for CREG12 transport calculations is preserved at https://github.com/meom-group/CDFTOOLS, available via under the CeCILL license (http://www.cecill.info/licences/Licence_CeCILL_V2-en.html) and developed openly at GitHub. The OSTIA satellite SST and sea ice data used for comparison with model output in the study are available at Copernicus Marine Services via https://doi.org/10.48670/moi-00168 with Open access and registration. The AW transport observation data used for validation of the model output in the study are available at the Norwegian Marine Data Centre via http://metadata.nmdc.no/metadata-api/landing-page/ce3d486edd053c2eff2508f3ef392bb4 with Creative Commons Attribution 4.0 International License without registration. The EN.4.2.2 data used for observational watermass property analysis in the study are available at Met Office Hadley Centre observations data sets via https://www.metoffice.gov.uk/hadobs/en4/ with Crown Copyright, Met Office provided under a Non-Commercial Government License (http://www.nationalarchives.gov.uk/doc/non-commercial-government-licence/version/2/).

Acknowledgments
This project was funded through the joint UK-France PhD program by DGA/Dstl, and overseen by Carole Nahum and Timothy Clarke. Additional support for this research was provided through the NERC-BMBF Changing Arctic Ocean Grant NE/R01275X/1, the NERC ArctiCONNECT grant NE/V005855/1 and the NERC CANARI Grant NE/W004984/1. The pan-Arctic simulation was performed using HPC resources from the french GENCI-CINES center (Grant 2018-A0050107420).

References

Aksenov, Y., Bacon, S., Coward, A. C., & Nurser, A. J. G. (2010). The North Atlantic inflow to the Arctic Ocean: High-resolution model study. *Journal of Marine Systems*, *79*(1–2), 1–22. https://doi.org/10.1016/j.jmarsys.2009.05.003

Antonov, J. I., Seidov, D., Boyer, T. P., Locarnini, R. A., Mishonov, A. V., Garcia, H. E., et al. (2010). Volume 2: Salinity. *World Ocean Atlas 2009*, *2*, 184.

Årthun, M., Eldevik, T., & Smedsrud, L. H. (2019). The role of Atlantic heat transport in future Arctic winter sea ice loss. *Journal of Climate*, *32*(11), 3327–3341. https://doi.org/10.1175/JCLI-D-18-0750.1

Årthun, M., Eldevik, T., Smedsrud, L. H., Skagseth, Ø., & Ingvaldsen, R. B. (2012). Quantifying the influence of Atlantic heat on Barents Sea ice variability and retreat. *Journal of Climate*, *25*(13), 4736–4743. https://doi.org/10.1175/JCLI-D-11-00466.1

Årthun, M., Ingvaldsen, R. B., Smedsrud, L. H., & Schrum, C. (2011). Dense water formation and circulation in the Barents Sea. *Deep-Sea Research Part I Oceanographic Research Papers*, *58*(8), 801–817. https://doi.org/10.1016/j.dsr.2011.06.001

Årthun, M., & Schrum, C. (2010). Ocean surface heat flux variability in the Barents Sea. *Journal of Marine Systems*, *83*(1–2), 88–98. https://doi.org/10.1016/j.jmarsys.2010.07.003

Barnier, B., Madec, G., Penduff, T., Molines, J. M., Treguier, A. M., Le Sommer, J., et al. (2006). Impact of partial steps and momentum advection schemes in a global ocean circulation model at eddy-permitting resolution. *Ocean Dynamics*, *56*(5–6), 543–567. https://doi.org/10.1007/s10236-006-0082-1

Barton, B. I., Lenn, Y.-D., & Lique, C. (2018). Observed atlantification of the Barents Sea Polar Front limits the expansion of winter sea ice. *Journal of Physical Oceanography*, *48*(8), 1849–1866. https://doi.org/10.1175/JPO-D-18-0003.1

Barton, B. I., Lique, C., & Lenn, Y.-D. (2020). Water mass properties derived from satellite observations in the Barents Sea. *Journal of Geophysical Research: Oceans*, *125*(8), e2019JC015449. https://doi.org/10.1029/2019JC015449

Blackport, R., & Screen, J. A. (2021). Observed statistical connections overestimate the causal effects of Arctic sea ice changes on midlatitude winter climate. *Journal of Climate*, *34*(8), 3021–3038. https://doi.org/10.1175/JCLI-D-20-0293.1

Blackport, R., Screen, J. A., van der Wiel, K., & Bintanja, R. (2019). Minimal influence of reduced Arctic sea ice on coincident cold winters in mid-latitudes. *Nature Climate Change*, *1–9*(9), 697–704. https://doi.org/10.1038/s41558-019-0551-4

Brodeau, L., Barnier, B., Treguier, A. M., Penduff, T., & Gulev, S. (2010). An ERA40-based atmospheric forcing for global ocean circulation models. *Ocean Modelling*, *31*(3–4), 88–104. https://doi.org/10.1016/j.ocemod.2009.10.005

de Lavergne, C., Falahat, S., Madec, G., Roquet, F., Nycander, J., & Vic, C. (2019). Toward global maps of internal tide energy sinks. *Ocean Modelling*, *137*, 52–75. https://doi.org/10.1016/j.ocemod.2019.03.010

Donlon, C. J., Martin, M., Stark, J., Roberts-Jones, J., Fiedler, E., & Wimmer, W. (2012). The operational sea surface temperature and sea ice analysis (OSTIA) system. *Remote Sensing of Environment*, *116*, 140–158. https://doi.org/10.1016/j.rse.2010.10.017

Dupont, F., Higginson, S., Bourdallé-Badie, R., Lu, Y., Roy, F., Smith, G. C., et al. (2015). A high-resolution ocean and sea-ice modelling system for the Arctic and North Atlantic Oceans. *Geoscientific Model Development*, *8*(5), 1577–1594. https://doi.org/10.5194/gmd-8-1577-2015

Fahrbach, E., Meincke, J., Österhus, S., Rohardt, G., Schauer, U., Tverberg, V., et al. (2001). Direct measurements of heat and mass transports through the Fram Strait. *Polar Research*, *20*(2), 217–224. https://doi.org/10.1111/j.1751-8369.2001.tb00059.x

Fossheim, M., Primicerio, R., Johannesen, E., Ingvaldsen, R. B., Aschan, M. M., & Dolgov, A. V. (2015). Recent warming leads to a rapid borealization of fish communities in the Arctic. *Nature Climate Change*, *5*(7), 673–677. https://doi.org/10.1038/nclimate2647

Gammelsrød, T., Leikvin, Ø., Lien, V., Budgell, W. P., Loeng, H., & Maslowski, W. (2009). Mass and heat transports in the NE Barents Sea: Observations and models. *Journal of Marine Systems*, *75*(1–2), 56–69. https://doi.org/10.1016/j.jmarsys.2008.07.010

Gawarkiewicz, G., & Plueddemann, A. J. (1995). Topographic control of thermohaline frontal structure in the Barents Sea polar front on the South flank of Spitsbergen bank. *Journal of Geophysical Research*, *100*(C3), 4509–4524. https://doi.org/10.1029/94jc02427

Gillard, L. C., Hu, X., Myers, P. G., & Bamber, J. L. (2016). Meltwater pathways from marine terminating glaciers of the Greenland ice sheet. *Geophysical Research Letters*, *43*(20), 10873–10882. https://doi.org/10.1002/2016GL070969

Gong, T., & Luo, D. (2017). Ural blocking as an amplifier of the Arctic sea ice decline in winter. *Journal of Climate*, *30*(7), 2639–2654. https://doi.org/10.1175/JCLI-D-16-0548.1

Gouretski, V., & Reseghetti, F. (2010). On depth and temperature biases in bathythermograph data: Development of a new correction scheme based on analysis of a global ocean database. *Deep-Sea Research Part I Oceanographic Research Papers*, *57*(6), 812–833. https://doi.org/10.1016/j.dsr.2010.03.011

Herbaut, C., Houssais, M.-N., Close, S., & Blaizot, A.-C. (2015). Two wind-driven modes of winter sea ice variability in the Barents Sea. *Deep-Sea Research Part I Oceanographic Research Papers*, *106*, 97–115. https://doi.org/10.1016/j.dsr.2015.10.005

Holliday, N. P., Bersch, M., Berx, B., Chafik, L., Cunningham, S., Florindo-López, C., et al. (2020). Ocean circulation causes the largest freshening event for 120 years in eastern subpolar North Atlantic. *Nature Communications*, *11*(1), 585. https://doi.org/10.1038/s41467-020-14474-y

Hoshi, K., Ukita, J., Honda, M., Nakamura, T., Yamazaki, K., Miyoshi, Y., & Jaiser, R. (2019). Weak stratospheric polar vortex events modulated by the Arctic sea ice loss. *Journal of Geophysical Research: Atmospheres*, *124*(2), 858–869. https://doi.org/10.1029/2018JD029222

Ingvaldsen, R. B., Asplin, L., & Loeng, H. (2004a). The seasonal cycle in the Atlantic transport to the Barents Sea during the years 1997-2001. *Continental Shelf Research*, *24*(9), 1015–1032. https://doi.org/10.1016/j.csr.2004.02.011

Ingvaldsen, R. B., Asplin, L., & Loeng, H. (2004b). Velocity field of the Western entrance to the Barents Sea. *Journal of Geophysical Research*, *109*(C3), 1–12. https://doi.org/10.1029/2003JC001811

Ingvaldsen, R. B., Assmann, K. M., Primicerio, R., Fossheim, M., Polyakov, I. V., & Dolgov, A. V. (2021). Physical manifestations and ecological implications of Arctic Atlantification. *Nature Reviews Earth & Environment*, *2*(12), 874–889. https://doi.org/10.1038/s43017-021-00228-x

Karcher, M., Beszczynska-Möller, A., Kauker, F., Gerdes, R., Heyen, S., Rudels, B., & Schauer, U. (2011). Arctic Ocean warming and its consequences for the Denmark Strait overflow. *Journal of Geophysical Research*, *116*(C2), 1–10. https://doi.org/10.1029/2010JC006265

Le Bras, I., Straneo, F., Muilwijk, M., Smedsrud, L. H., Li, F., Susan Lozier, M., & Penny Holliday, N. (2021). How much arctic fresh water participates in the subpolar overturning circulation? *Journal of Physical Oceanography*, *51*(3), 955–973. https://doi.org/10.1175/JPO-D-20-0240.1

Levitus, S., Matishov, G., Seidov, D., & Smolyar, I. (2009). Barents Sea multidecadal variability. *Geophysical Research Letters*, *36*(19), 1–5. https://doi.org/10.1029/2009GL039847

Lind, S., Ingvaldsen, R. B., & Furevik, T. (2016). Arctic layer salinity controls heat loss from deep Atlantic layer in seasonally ice-covered areas of the Barents Sea. *Geophysical Research Letters*, *43*(10), 5233–5242. https://doi.org/10.1002/2016GL068421

Lind, S., Ingvaldsen, R. B., & Furevik, T. (2018). Arctic warming hotspot in the northern Barents Sea linked to declining sea-ice import. *Nature Climate Change*, *8*(7), 634–639. https://doi.org/10.1038/s41558-018-0205-y

Lique, C., Johnson, H. L., & Plancherel, Y. (2018). Emergence of deep convection in the Arctic Ocean under a warming climate. *Climate Dynamics*, *50*(9–10), 1–15. https://doi.org/10.1007/s00382-017-3849-9

Locarnini, R. A., Mishonov, A. V., Antonov, J. I., Boyer, T. P., Garcia, H. E., Baranova, O. K., et al. (2010). Volume 1: Temperature. *World Ocean Atlas 2009*, *1*, 182. Retrieved from http://www.ncbi.nlm.nih.gov/pubmed/22058116

Loeng, H. (1991). Features of the physical oceanograpic conditions of the Barents Sea. *Polar Research*, *10*(1), 5–18. https://doi.org/10.1111/j.1751-8369.1991.tb00630.x

Luo, D., Xiao, Y., Yao, Y., Dai, A., Simmonds, I., & Franzke, C. L. (2016). Impact of ural blocking on winter warm Arctic-cold Eurasian anomalies. Part I: Blocking-induced amplification. *Journal of Climate*, *29*(11), 3925–3947. https://doi.org/10.1175/JCLI-D-15-0611.1

Madec, G., & The_NEMO_Team. (2008). NEMO ocean engine (Technical Report No. 27). Pôle de môdellisation, Institute Pierre Simon Laplace. Retrieved from http://www.nemo-ocean.eu/About-NEMO/Reference-manuals$%5C$npapers2://publication/uuid/73E7FF17-99BE-4B10-A823-0037C823EF6E

Mann, M. E., Steinman, B. A., & Miller, S. K. (2020). Absence of internal multidecadal and interdecadal oscillations in climate model simulations. *Nature Communications*, *11*(1), 1–9. https://doi.org/10.1038/s41467-019-13823-w

Maslowski, W., Marble, D., Walczowski, W., Schauer, U., Clement, J. L., & Semtner, A. J. (2004). On climatological mass, heat, and salt transports through the Barents Sea and Fram Strait from a pan-Arctic coupled ice-ocean model simulation. *Journal of Geophysical Research*, *109*(C3), C03032. https://doi.org/10.1029/2001JC001039

McCrystall, M. R., & Screen, J. A. (2021). Arctic winter temperature variations correlated with ENSO are dependent on coincidental sea ice changes. *Geophysical Research Letters*, *48*(8), 1–11. https://doi.org/10.1029/2020GL091519

Meneghello, G., Marshall, J., Lique, C., Isachsen, P. E., Doddridge, E., Campin, J. M., et al. (2021). Genesis and decay of mesoscale baroclinic eddies in the seasonally ice-covered interior arctic ocean. *Journal of Physical Oceanography*, *51*(1), 115–129. https://doi.org/10.1175/JPO-D-20-0054.1

Nurser, A. J., & Bacon, S. (2014). The rossby radius in the Arctic Ocean. *Ocean Science*, *10*(6), 967–975. https://doi.org/10.5194/os-10-967-2014

Nurser, A. J., Marsh, R., & Williams, R. G. (1999). Diagnosing water mass formation from air-sea fluxes and surface mixing. *Journal of Physical Oceanography*, *29*(7), 1468–1487. https://doi.org/10.1175/1520-0485(1999)029<1468:dwmffa>2.0.co;2

Onarheim, I. H., & Årthun, M. (2017). Toward an ice-free Barents Sea. *Geophysical Research Letters*, *44*(16), 8387–8395. https://doi.org/10.1002/2017GL074304

Onarheim, I. H., Eldevik, T., Årthun, M., Ingvaldsen, R. B., & Smedsrud, L. H. (2015). Skillful prediction of Barents Sea ice cover. *Geophysical Research Letters*, *42*(13), 5364–5371. https://doi.org/10.1002/2015GL064359.Abstract

Onarheim, I. H., Eldevik, T., Smedsrud, L. H., & Stroeve, J. C. (2018). Seasonal and regional manifestation of Arctic sea ice loss. *Journal of Climate*, *31*(12), 4917–4931. https://doi.org/10.1175/JCLI-D-17-0427.1

Oziel, L., Sirven, J., & Gascard, J. C. (2016). The Barents Sea frontal zones and water masses variability (1980–2011). *Ocean Science*, *12*(1), 169–184. https://doi.org/10.5194/os-12-169-2016

Petoukhov, V., & Semenov, V. A. (2010). A link between reduced Barents-Kara sea ice and cold winter extremes over northern continents. *Journal of Geophysical Research*, *115*(21), 1–11. https://doi.org/10.1029/2009JD013568

Regan, H., Lique, C., Talandier, C., & Meneghello, G. (2020). Response of total and eddy kinetic energy to the recent spinup of the Beaufort Gyre. *Journal of Physical Oceanography*, *50*(3), 575–594. https://doi.org/10.1175/JPO-D-19-0234.1

Rousset, C., Vancoppenolle, M., Madec, G., Fichefet, T., Flavoni, S., Barthélemy, A., et al. (2015). The Louvain-La-Neuve sea ice model LIM3.6: Global and regional capabilities. *Geoscientific Model Development*, *8*(10), 2991–3005. https://doi.org/10.5194/gmd-8-2991-2015

Rudels, B., Muench, R. D., Gunn, J., Schauer, U., & Friedrich, H. J. (2000). Evolution of the Arctic Ocean boundary current north of the Siberian shelves. *Journal of Marine Systems*, *25*(1), 77–99. https://doi.org/10.1016/S0924-7963(00)00009-9

Schauer, U., Loeng, H., Rudels, B., Ozhigin, V. K., & Dieck, W. (2002). Atlantic Water flow through the Barents and Kara Seas. *Deep-Sea Research Part I Oceanographic Research Papers*, *49*(12), 2281–2298. https://doi.org/10.1016/S0967-0637(02)00125-5

Schlichtholz, P. (2019). Subsurface ocean flywheel of coupled climate variability in the Barents Sea hotspot of global warming. *Scientific Reports*, *9*(1), 1–16. https://doi.org/10.1038/s41598-019-49965-6

Serreze, M. C., Barrett, A. P., Slater, A. G., Steele, M., Zhang, J., & Trenberth, K. E. (2007). The large-scale energy budget of the Arctic. *Journal of Geophysical Research*, *112*(11), 1–17. https://doi.org/10.1029/2006JD008230

Serreze, M. C., Barrett, A. P., Slater, A. G., Woodgate, R. A., Aagaard, K., Lammers, R. B., et al. (2006). The large-scale freshwater cycle of the Arctic. *Journal of Geophysical Research*, *111*(11), 1–19. https://doi.org/10.1029/2005JC003424

Skagseth, Ø. (2008). Recirculation of Atlantic Water in the Western Barents Sea. *Geophysical Research Letters*, *35*(11), 1–5. https://doi.org/10.1029/2008GL033785

Skagseth, Ø., Drinkwater, K. F., & Terrile, E. (2011). Wind-and buoyancy-induced transport of the Norwegian coastal current in the Barents Sea. *Journal of Geophysical Research*, *116*(8), C08007. https://doi.org/10.1029/2011JC006996

Skagseth, Ø., Eldevik, T., Årthun, M., Asbjørnsen, H., Lien, V. S., & Smedsrud, L. H. (2020). Reduced efficiency of the Barents Sea cooling machine. *Nature Climate Change*, *10*(7), 661–666. https://doi.org/10.1038/s41558-020-0772-6

Skagseth, Ø., Furevik, T., Ingvaldsen, R. B., Loeng, H., Mork, K. A., Orvik, K. A., & Ozhigin, V. (2008). Volume and heat transport to the Arctic Ocean via the Norwegian and Barents Seas. In R. R. Dickson, J. Meincke, & P. Rhines (Eds.), *Arctic-subarctic ocean fluxes: Defining the role of the northern seas in climate* (pp. 45–64). Springer. https://doi.org/10.1007/978-1-4020-6774-7

Smedsrud, L. H., Esau, I., Ingvaldsen, R. B., Eldevik, T., Haugan, P. M., Li, C., et al. (2013). The role of the Barents Sea in the Arctic climate system. *Reviews of Geophysics*, *51*(3), 415–449. https://doi.org/10.1002/rog.20017

Smedsrud, L. H., Ingvaldsen, R., Nilsen, J. E. Ø., & Skagseth, Ø. (2010). Heat in the Barents Sea: Transport, storage, and surface fluxes. *Ocean Science*, *6*(1), 219–234. https://doi.org/10.5194/os-6-219-2010

Talandier, C., & Lique, C. (2021). CREG12.L75-REF08. https://doi.org/10.5281/zenodo.5789520

Treguier, A. M., Deshayes, J., Le Sommer, J., Lique, C., Madec, G., Penduff, T., et al. (2014). Meridional transport of salt in the global ocean from an eddy-resolving model. *Ocean Science*, *10*(2), 243–255. https://doi.org/10.5194/os-10-243-2014

Venegas, S. A., & Mysak, L. A. (2000). Is there a dominant timescale of natural climate variability in the Arctic? *Journal of Climate*, *13*(19), 3412–3434. https://doi.org/10.1175/1520-0442(2000)013<3412:itadto>2.0.co;2

Warner, J. L., Screen, J. A., & Scaife, A. A. (2020). Links Between Barents-Kara Sea ice and the extratropical atmospheric circulation explained by internal variability and tropical forcing. *Geophysical Research Letters*, *47*(1). https://doi.org/10.1029/2019GL085679

Wekerle, C., Wang, Q., Danilov, S., Schourup-Kristensen, V., von Appen, W.-J., & Jung, T. (2017). Atlantic Water in the Nordic Seas: Locally eddy-permitting ocean simulation in a global setup. *Journal of Geophysical Research: Oceans*, *122*(2), 914–940. https://doi.org/10.1002/2016JC012121.Received

Yashayaev, I., & Seidov, D. (2015). The role of the Atlantic Water in multidecadal ocean variability in the Nordic and Barents Seas. *Progress in Oceanography*, *132*, 68–127. https://doi.org/10.1016/j.pocean.2014.11.009